2D electrostatic modeling of twisted pairs

Kaoutar Hazim

*Laboratoire Systèmes Electrotechniques et Environnement (LSEE),
Artois University, Béthune, France and Department of Electrical Engineering and
Computer Science, Montefiore Institute, University of Liège, Liège, Belgium*

Guillaume Parent and Stéphane Duchesne

*Laboratoire Systèmes Electrotechniques et Environnement (LSEE),
Artois University, Béthune, France*

Andrè Nicolet

*CNRS, Centrale Marseille, Institut Fresnel, Aix-Marseille University,
Marseille, France, and*

Christophe Geuzaine

*Department of Electrical Engineering and Computer Science, Montefiore Institute,
University of Liège, Liège, Belgium*

Abstract

Purpose – This paper aims to model a three-dimensional twisted geometry of a twisted pair studied in an electrostatic approximation using only two-dimensional (2D) finite elements.

Design/methodology/approach – The proposed method is based on the reformulation of the weak formulation of the electrostatics problem to deal with twisted geometries only in 2D.

Findings – The method is based on a change of coordinates and enables a faster computational time as well as a high accuracy.

Originality/value – The effectiveness of the adopted approach is demonstrated by studying different configurations related to the IEC 60851-5 standard defined for the measurement of the electrical properties of the insulation of the winding wires used in electrical machines.

Keywords Applied electromagnetism, Finite element method, Electrostatics, Finite elements, Helicoidal coordinates, Twisted geometry

Paper type Research paper

1. Introduction
Using twisted wires in electrical engineering goes back to the late 19th century, when Bell introduced them to mitigate the crosstalk between the first telephone and a telegraph

(Bell, 1876). They soon became commonplace in many electric and electronic applications and are in particular used as a means to test the aging of the insulation of electrical machines (Guastavino and Dardano, 2012) and to extract the electrical properties of their insulation (IEC, 2019).

Several studies have investigated the effect of twisted wires on the surrounding environment (Moser and Spencer, 1968), a nearby single wire (Paul and Jolly, 1982) or the ground (Pignari and Spadacini, 2011), by using predictive models. However, the accurate calculation of the distributed capacitances or the local electromagnetic fields, e.g. the local electric field strength for realistic configurations, requires costly three-dimensional (3D) simulations (Acero *et al.*, 2014; Lyly *et al.*, 2012). While a method based on several two-dimensional (2D) simulations (on slices of the 3D geometry) was proposed in Gustavsen *et al.* (2009), it introduces an intrinsic modeling error because of the performed averaging and cannot recover the true 3D local fields.

In this paper, following the approach originally derived in Nicolet *et al.* (2006, 2007a), we propose to reformulate the 3D problem in helicoidal instead of Cartesian coordinates (Waldron, 1958), leading to a 2D formulation with an adapted metric, easy to implement in existing 2D finite element codes. For purely helicoidal and infinitely long 3D geometries, the proposed 2D formulation is exact. The gains are twofold: the geometrical modeling and meshing of the potentially complex multi-layer conductors usually with large aspect ratios can be performed on a 2D slice instead of in 3D; and the finite element solution is greatly reduced.

The paper is organized as follows. After describing the geometrical configuration of twisted pairs in Section 2, the 3D electrostatic problem is reformulated in helicoidal coordinates in Section 3, leading to a 2D finite element formulation with an adapted metric – the "2D twisted" model. This 2D twisted model is verified against the full 3D model in Section 4 by computing the conductor charges in function of the number of turns in a twisted pair of enameled wires. Next, the improvement in accuracy of the 2D twisted model compared to the usual 2D (straight) model is analyzed in Section 5 in function of the number of turns, the conductor diameter and the insulation thickness. The effectiveness of the approach is finally demonstrated by studying different configurations related to the IEC 60851-5 standard for the measurement of the electrical properties of winding wires.

2. Geometry of twisted wires

The twisted geometry is defined by a number of turns N_{turns} over a swirl length ℓ_s (Figure 1). One spatial period of the twisted pair is depicted in Figure 2, where the extrusion length ℓ_e (i.e. the linear length of the spatial period) and the length of the helix ℓ_h (i.e. the length of the mean fiber of each twisted conductor) are defined as follows:
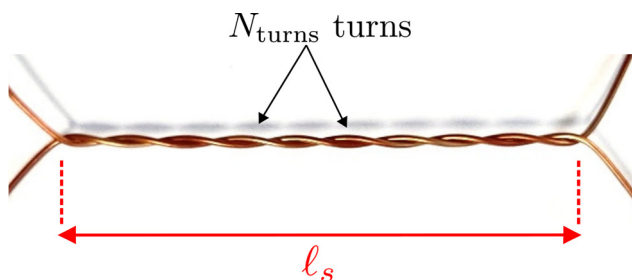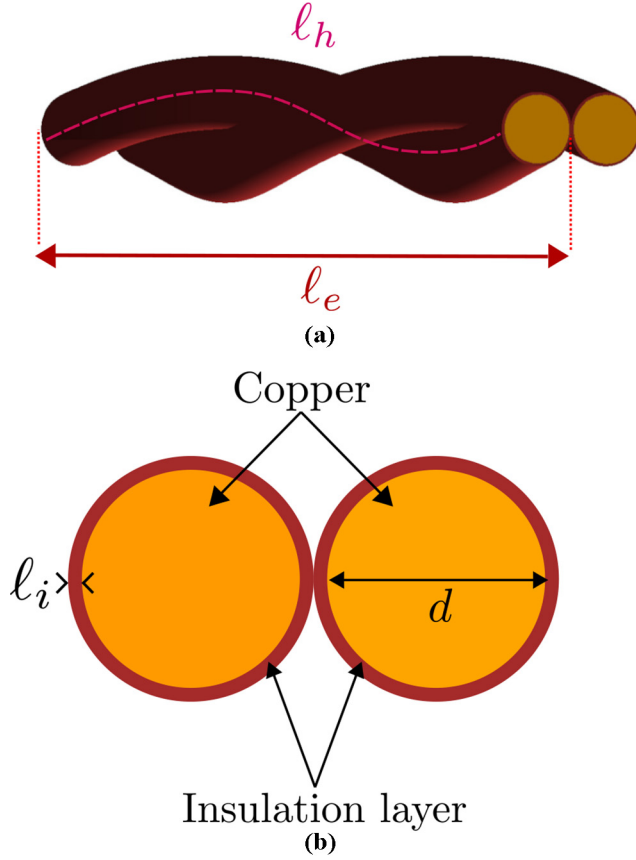

N_{turns} turns

ℓ_s

$$\begin{cases} \ell_e = \dfrac{\ell_s}{N_{\text{turns}}} \\ \ell_h = \sqrt{(\pi(d + 2\ell_i))^2 + \ell_e^2} \end{cases} \tag{1}$$

with d and ℓ_i being the diameter of the conductors and the insulation thickness, respectively. Finally, the torsion of the twisted pair is defined as $\alpha = \frac{2\pi}{\ell_e}$.

3. Twisted electrostatic model
To study the capacitive coupling between the twisted wires using the finite element method, we first derive a weak form of Maxwell's equations in the electrostatic approximation.

3.1 Electrostatic model
Assuming zero free charge density, and denoting the (static) electric field and the dielectric permittivity in Cartesian coordinates (x_1, x_2, x_3), respectively, by e(x_1, x_2, x_3) and $\varepsilon(x_1, x_2, x_3)$, Maxwell's equations reduce to:

$$\mathbf{curl}_x(\mathbf{e}) = 0, \quad \mathbf{div}_x(\varepsilon\,\mathbf{e}) = 0, \tag{2}$$

where $\mathbf{curl}_x$ and $\mathbf{div}_x$ are the classical curl and divergence operators in the Cartesian coordinates system, respectively. Defining the scalar electric potential $v(x_1, x_2, x_3)$ such that $\mathbf{e} = -\mathbf{grad}_x(v)$, (2) leads to the second-order equation as follows:

$$-\mathbf{div}_x(\varepsilon\,\mathbf{grad}_x(v)) = 0, \tag{3}$$

where $\mathbf{grad}_x$ denotes the gradient operator in Cartesian coordinates.

Our aim is to solve (3) in a domain Ω_x enclosing the twisted pair, with a prescribed scalar potential on the (boundary of the) conductors. To use the finite element method, Ω_x is bounded and an appropriate geometrical transformation is defined in an annular region to handle the natural extension of fields to infinity (Henrotte *et al.*, 1999; Remacle *et al.*, 1994; Bossavit, 1998). The annular region (of inner and outer radii R_{int} and R_{out}, respectively) is depicted in Figure 3. The boundary $\partial\,\Omega_x$ of Ω_x is thus composed of the boundary of the conductors in the twisted pair Γ_c and the outside boundary of the annular region Γ_{out}.

3.2 Weak formulation in Cartesian coordinates

Let us assume that the potential v is fixed to zero on Γ_{out} and to a prescribed value $v_c(x_1, x_2, x_3)$ on Γ_c. The weak formulation of (3) writes (Ern and Guermond, 2013): find $v \in H^1(\Omega_x)$ with $v = v_c$ on Γ_c and $v = 0$ on Γ_{out}, such that:

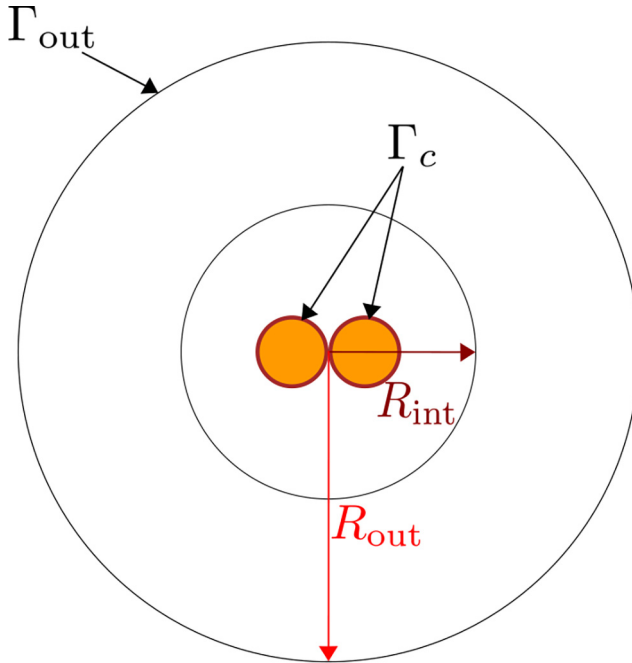$$\int_{\Omega_x} \varepsilon\,\mathbf{grad}_x(v) \cdot \mathbf{grad}_x(v')d\Omega_x = 0 \tag{4}$$

Figure 3.
Bounded domain with annular region with geometrical transformation to handle the natural extension of fields to infinity

holds for all test functions $v' \in H_0^1(\Omega_x)$. Here, $H^1(\Omega_x)$ denotes the classical Sobolev space on Ω_x, and $H_0^1(\Omega_x)$ its subspace with functions vanishing on the boundary $\partial \Omega_x$. For the 3D geometry, periodic boundary conditions along the x_3 axis are used. After discretizing Ω_x with a finite element mesh, and choosing suitable finite dimensional subspaces (e.g. with piecewise linear or quadratic shape functions), (4) becomes:

$$\int_{\Omega_x} \left(\varepsilon \, \mathbf{grad}_x(v_h) \right)^{\mathrm{T}} \mathbf{grad}_x\left(v'_h\right) d\Omega_x = 0, \tag{5}$$

where the superscript "T" denotes the transpose, whereas v_h and v'_h denote the finite dimensional approximation of v and v', respectively, leading thus to the classical matrix system.

Following the approach described in Nicolet *et al.* (2006, 2007a), we now reformulate the weak formulation (5) in helicoidal coordinates.

3.3 Helicoidal coordinates

Helicoidal coordinates $(\zeta_1, \zeta_2, \zeta_3)$ are related to the Cartesian coordinates (x_1, x_2, x_3) through the following relations (Figure 4) (Waldron, 1958):

$$\begin{cases} x_1 = \zeta_1 \cos(\alpha\zeta_3) + \zeta_2 \sin(\alpha\zeta_3) \\ x_2 = -\zeta_1 \sin(\alpha\zeta_3) + \zeta_2 \cos(\alpha\zeta_3), \\ x_3 = \zeta_3 \end{cases} \tag{6}$$
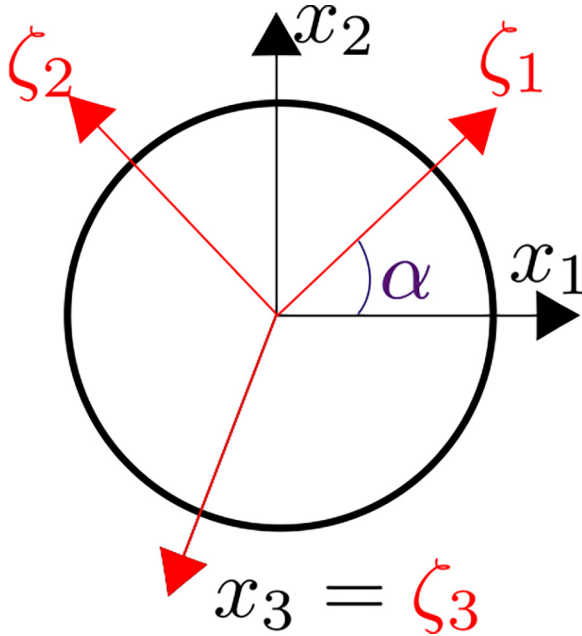

Figure 4.
Definition of Cartesian and helicoidal coordinates

or, conversely:

$$\begin{cases} \zeta_1 = x_1\cos(\alpha x_3) - x_2\sin(\alpha x_3) \\ \zeta_2 = x_1\sin(\alpha x_3) + x_2\cos(\alpha x_3) \, . \\ \zeta_3 = x_3 \end{cases} \tag{7}$$

The Jacobian of the transformation from helicoidal to Cartesian coordinates is defined as follows:

$$\mathbf{J} = \frac{\partial(x_1, x_2, x_3)}{\partial(\zeta_1, \zeta_2, \zeta_3)} = \begin{pmatrix} \dfrac{\partial x_1}{\partial \zeta_1} & \dfrac{\partial x_1}{\partial \zeta_2} & \dfrac{\partial x_1}{\partial \zeta_3} \\ \dfrac{\partial x_2}{\partial \zeta_1} & \dfrac{\partial x_2}{\partial \zeta_2} & \dfrac{\partial x_2}{\partial \zeta_3} \\ \dfrac{\partial x_3}{\partial \zeta_1} & \dfrac{\partial x_3}{\partial \zeta_2} & \dfrac{\partial x_3}{\partial \zeta_3} \end{pmatrix}, \tag{8}$$

which, using (6), writes:

$$\mathbf{J} = \begin{pmatrix} \cos(\alpha\zeta_3) & \sin(\alpha\zeta_3) & \alpha\zeta_2\cos(\alpha\zeta_3) - \alpha\zeta_1\sin(\alpha\zeta_3) \\ -\sin(\alpha\zeta_3) & \cos(\alpha\zeta_3) & -\alpha\zeta_1\cos(\alpha\zeta_3) - \alpha\zeta_2\sin(\alpha\zeta_3) \\ 0 & 0 & 1 \end{pmatrix}. \tag{9}$$

If $\mathbf{grad}_\zeta$ denotes the gradient in helicoidal coordinates and $\mathbf{J}^{-T}$ the inverse of the transpose of $\mathbf{J}$, we have:

$$\mathbf{grad}_x(v_h) = \mathbf{J}^{-T}\mathbf{grad}_\zeta(v_h), \tag{10}$$

and the weak form (5) in helicoidal coordinates becomes (because $d\Omega_x = \det(\mathbf{J})d\Omega_\zeta$: find v_h such that:

$$\int_{\Omega_\zeta} \left(\varepsilon\, \mathbf{J}^{-T}\, \mathbf{grad}_\zeta(v_h) \right)^T \mathbf{J}^{-T}\mathbf{grad}_\zeta\left(v_h'\right)\det(\mathbf{J})\, d\Omega_\zeta = 0$$
$$\Rightarrow \int_{\Omega_\zeta} \varepsilon\, \mathbf{grad}_\zeta(v_h)^T \mathbf{J}^{-1}\, \mathbf{J}^{-T}\, \mathbf{grad}_\zeta\left(v_h'\right)\det(\mathbf{J})\, d\Omega_\zeta = 0 \tag{11}$$

where Ω_ζ refers to the domain of study in helicoidal coordinates. Equation (11) can be further simplified as follows:

$$\Rightarrow \int_{\Omega_\zeta} \varepsilon\, \mathbf{grad}_\zeta(v_h)^T\, \mathbf{T}^{-1}\, \mathbf{grad}_\zeta\left(v_h'\right) d\Omega_\zeta = 0, \tag{12}$$

with $\mathbf{T}^{-1}$ the symmetric matrix:

$$\begin{aligned} \mathbf{T}^{-1}(\zeta_1, \zeta_2) &= \mathbf{T}^{-T}(\zeta_1, \zeta_2) \\ &= \mathbf{J}^{-1}\mathbf{J}^{-T}\det(\mathbf{J}) \\ &= \begin{pmatrix} 1 + \alpha^2\zeta_2^2 & -\alpha^2\zeta_1\zeta_2 & -\alpha\zeta_2 \\ -\alpha^2\zeta_1\zeta_2 & 1 + \alpha^2\zeta_1^2 & \alpha\zeta_1 \\ -\alpha\zeta_2 & \alpha\zeta_1 & 1 \end{pmatrix}, \end{aligned} \tag{13}$$

thus making (12) become:

$$\int_{\Omega_\zeta} \left(\varepsilon \mathbf{T}^{-1} \, \mathbf{grad}_\zeta \, (v_h)\right)^{\mathrm{T}} \mathbf{grad}_\zeta \, (v'_h) \, d\Omega_\zeta = 0. \tag{14}$$

Formally, comparing (5) to (14), the dielectric material represented by the scalar permittivity ε in Cartesian coordinates is thus replaced in helicoidal coordinates by an equivalent anisotropic and inhomogeneous permittivity tensor density $\varepsilon \mathrm{T}^{-1}$ (Nicolet *et al.*, 2007a, 2007b). The matrix $\mathrm{T}^{-1}(\zeta_1, \zeta_2)$ being independent of ζ_3, (14) can be reduced to a 2D problem in terms of coordinates ζ_1 and ζ_2, on a "slice" of the 3D geometry with constant $\zeta_3 = x_3$, without information loss. When expressed in polar coordinates (ρ, ϕ) defined as follows:

$$\begin{cases} \zeta_1 = \rho \cos(\phi) \\ \zeta_2 = \rho \sin(\phi) \end{cases}, \tag{15}$$

with $\phi = 2\arctan\left(\frac{\zeta_2}{\zeta_1 + \sqrt{\zeta_1^2 + \zeta_2^2}}\right)$, $\mathbf{T}^{-1}$ can be rewritten as follows:

$$\mathbf{T}^{-1}(\zeta_1, \zeta_2) = \mathbf{R}(\phi) \begin{pmatrix} 1 & 0 & 0 \\ 0 & 1 + \alpha^2 \rho^2 & \alpha \rho \\ 0 & \alpha \rho & 1 \end{pmatrix} \mathbf{R}(-\phi), \tag{16}$$

where $\mathbf{R}(\phi)$ is the rotation matrix:

$$\mathbf{R}(\phi) = \begin{pmatrix} \cos(\phi) & -\sin(\phi) & 0 \\ \sin(\phi) & \cos(\phi) & 0 \\ 0 & 0 & 1 \end{pmatrix}. \tag{17}$$

As mentioned in Section 3.1, the domain of study is bounded by an annular region of inner and outer radii R_{int} and R_{out}, respectively, to handle the natural extension of fields to infinity. The matrix is thus piecewise defined, with (16) being valid for $\rho \leq R_{\text{int}}$. The expression of the matrix for $\rho \in]R_{\text{int}}, R_{\text{out}}]$ is presented next.

3.4 Infinite transformation
In the annular region $\rho \in]R_{\text{int}}, R_{\text{out}}]$, a geometrical transformation is applied to handle the natural extension of the fields to infinity (Henrotte *et al.*, 1999; Remacle *et al.*, 1994), and the matrix $\mathbf{T}^{-1}$ writes:

$$\mathbf{T}^{-1}(\zeta_1, \zeta_2) = \mathbf{R}(\phi) \begin{pmatrix} \dfrac{\mathrm{r}}{\mathrm{d_r}\rho} & 0 & 0 \\ 0 & (1 + \alpha^2 \mathrm{r}^2)\dfrac{\mathrm{d_r}\rho}{\mathrm{r}} & \alpha \mathrm{d_r r} \\ 0 & \alpha \mathrm{d_r r} & \dfrac{\mathrm{d_r r}}{\rho} \end{pmatrix} \mathbf{R}(-\phi).$$

The parameters r and $\mathrm{d_r}$ are the transformed radial cylindrical coordinates and the derivative of r, respectively:

$$\begin{cases} r = r(\rho) = \dfrac{(R_{\text{int}} - R_{\text{out}})}{\rho - R_{\text{out}}} \rho \\ d_r = d_r(\rho) = \dfrac{\partial r}{\partial \rho} = -R_{\text{out}} \dfrac{R_{\text{int}} - R_{\text{out}}}{(\rho - R_{\text{out}})^2} \end{cases}. \tag{18}$$

The infinite transformation can be seen as a change in the physical properties of the "infinite air," thus an anisotropic and piecewise defined tensorial permittivity is used in the 2D finite element implementation.

4. Verification of the two-dimensional twisted model
Given the spatial periodicity of the geometry, only one spatial period referred to as the 3D geometry, with its cross section defining the 2D geometry is studied. For all geometries, created and meshed using Gmsh (Geuzaine and Remacle, 2009), an "infinite" transformation is applied in an annular region as described in Section 3.4. The 3D geometry was used to solve (5) and the 2D to solve (14). The finite element computations were performed using the open source finite element solver GetDP (Dular *et al.*, 1998a).

In real applications, enameled conductors are coated in successive thin layers to ensure correct polymerization and cross-linking. This defines the thermal and electrical performance of the wire. A classical arrangement is polyester-imide (PEI) as the first layer and polyamide-imide (PAI) on top. Additionally, for this case study the layers were given the same thickness. Thus, ε is defined as a piecewise function and its values were chosen for the two layers in 3D to be $\varepsilon_{\text{PEI}} = 4.5\varepsilon_0$ and $\varepsilon_{\text{PAI}} = 2.4\varepsilon_0$, where $\varepsilon_0 = \frac{1}{36\pi} 10^{-9} \text{F m}^{-1}$ is the vacuum permittivity, 4.5 and 2.4 being the relative permittivities of PEI and PAI, respectively. The equivalent anisotropic and inhomogeneous dielectric permittivity for the 2D twisted study is hence easily deduced (Section 3.3). This is portrayed in Figure 5, where a capacitor is used to illustrate the capacitive coupling between the two conductors.

To verify the 2D twisted model, simulations were run where the quantity of interest is the charge per meter Q of the system (Dular *et al.*, 1998b). Using finite elements, and for both geometries, the computation of the charges per meter is done as follows:

$$\begin{cases} \text{3D} \quad \text{case}: \ Q_{\text{3D}} = \dfrac{1}{\ell_e} \displaystyle\int_{\Gamma_c} \varepsilon \, \mathbf{grad}_x(v_h) \cdot \mathbf{n} \, d\Gamma_c \\ \text{2D} \quad \text{case}: \ Q_{\text{2D}_\alpha} = \displaystyle\int_{\Gamma_c} \varepsilon \mathbf{T}^{-1} \, \mathbf{grad}_\zeta(v_h) \cdot \mathbf{n} \, d\Gamma_c \end{cases}, \tag{19}$$
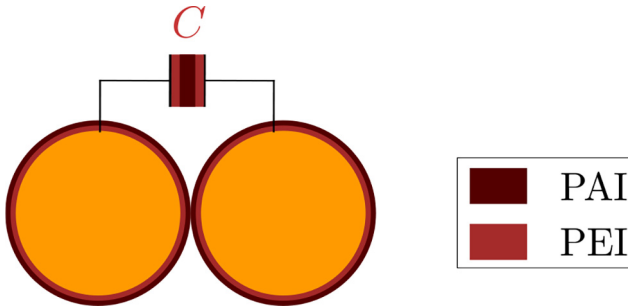

PAI
PEI

Figure 5.
Illustration of the capacitive coupling between the two conductors

where **n** is the outside normal to Γ_c, Q_{3D} is the charge computed in 3D converted to a 2D value by dividing by ℓ_e and Q_{2D_α} is the charge computed by the 2D twisted model.

Finite element computations were performed for a predefined range of N_{turns} per meter varying from 64 to 768, for a fixed value of ℓ_s. In all computations the potential difference between the two conductors was set to 1 V, and the potential at infinity was set to 0 V. The results are presented in Figure 6, where the corresponding 3D geometries were added to illustrate the amount of twist. The relative error used for comparison is defined as follows:

$$\text{error}(\%) = 100.\frac{|Q_{3D} - Q_{2D_\alpha}|}{Q_{3D}}.$$

As depicted in Figure 6(b), the relative error does not exceed 0.06%, which validates the twisted model. (The remaining small error is because of the small discrepancy between the 3D mesh and the exact twisted geometry.) The computational efficiency of the 3D and 2D models is reported in Table 1. The number of nodes in the 3D mesh is about 21 times the number of nodes in 2D mesh, which explains the large difference in the computational times: 16 min for the 3D model and only 8 s for the 2D model.
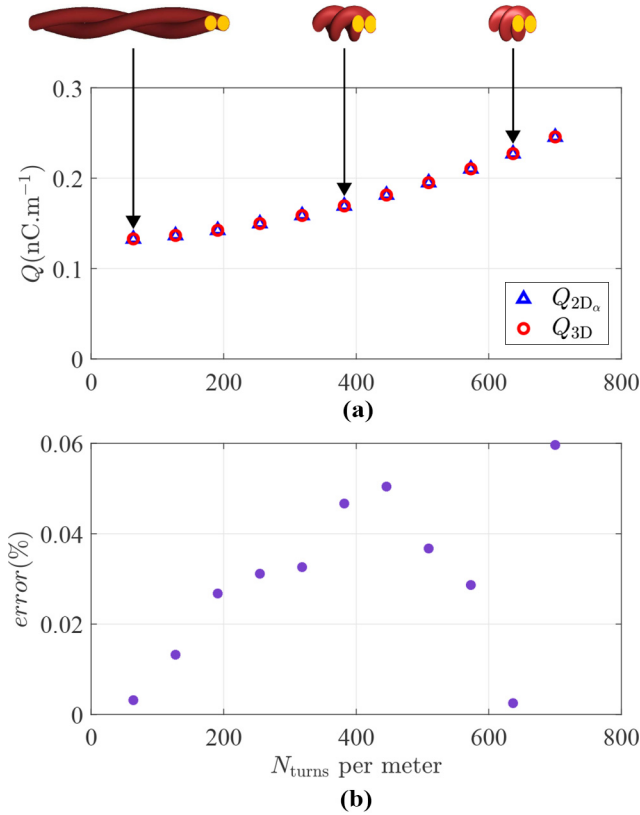

Figure 6.
(a) Comparison of the computed charges per meter for the 2D and 3D geometries. (b) The relative error between Q_{3D} and Q_{2D_α}

As noticed in Figure 6(a), the increase of N_{turns} yields an increase in the computed charge, which is because of the increase of the capacitive coupling between the different parts of the studied conductor. This extra capacity, referred to as C_s, is illustrated in Figure 7. The higher N_{turns}, the less air there is between the two electrodes of the equivalent capacitance C_s, the higher is the computed charge. It is also worth mentioning that for very high and non-physical values of N_{turns}, the relative error starts to increase, because of the increased deformation of the 3D mesh. Finally, it should also be noted that in addition to global quantities like the charge, the 2D model also allows to retrieve local quantities like the electric field strength.

5. Impact of the twisted geometry on the computed values

To emphasize the importance of using the proposed 2D twisted model instead of simplifying the study to a 2D straight model, we study the influence of the geometrical parameters N_{turns}, d and, ℓ_i over the computed charges Q_{2D_α} and Q_{2D_0}. The latter is the computed 2D charge for a straight geometry, i.e. with $\alpha = 0$.

5.1 Impact of the number of turns

To study the impact of the number of turns N_{turns} over the computed 2D charges, d was fixed to 0.8 mm, and ℓ_i to 28 μm. A new variable Q_{2D_α} is introduced corresponding to a corrected 2D twisted 2D charge deduced from a straight charge analytically, as follows:

$$Q_{\text{2D}_{\alpha_c}} = Q_{\text{2D}_0} \frac{\ell_h}{\ell_e} = Q_{\text{2D}_0} \sqrt{\left(\frac{\pi(d + 2\ell_i)}{\ell_e}\right)^2 + 1}, \qquad (20)$$

where ℓ_e and ℓ_h are defined in Figure 2. The results are plotted in Figure 8, where error$_1$ and error$_2$ are computed as in (21):

	2D	3D
No. of nodes	47,755	1,002,945
No. of elements	101,188	2,226,182
Computational time	8 s	16 min

Table 1.
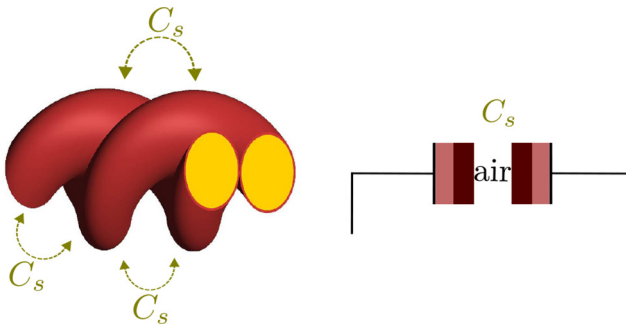Comparison of the computational efficiencies of the 2D and 3D models

Figure 7.
Figure portraying the new capacitive couplings C_s a twisted geometry presents
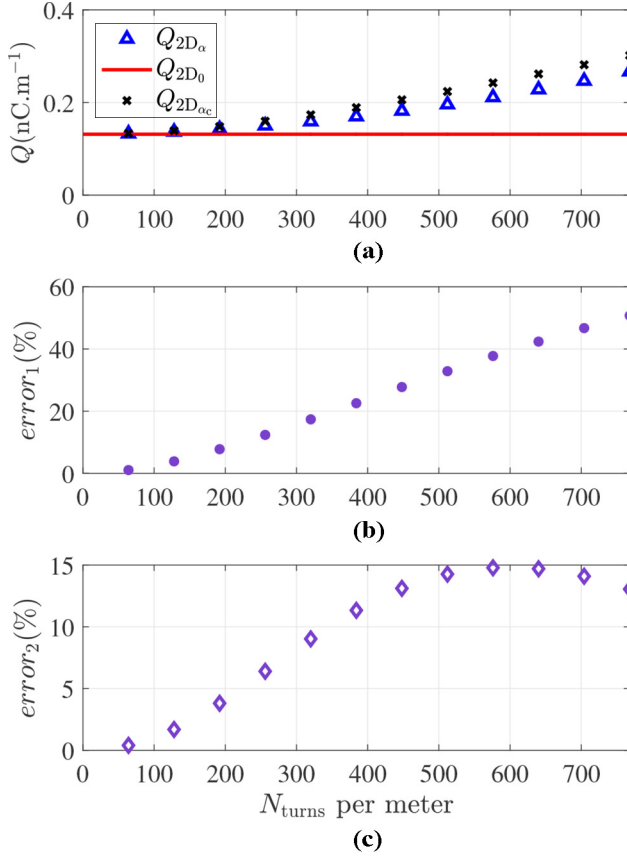
Figure 8.
(a) Study of the
impact of the number
of turns per meter on
Q_{2D_α}, Q_{2D_0} and $Q_{2D_{\alpha c}}$.
(b) The computed
relative error between
Q_{2D_α} and Q_{2D_0}.
(c) The computed
relative error between
Q_{2D_α} and $Q_{2D_{\alpha c}}$

$$\begin{cases} \text{error}_1(\%) = 100. \dfrac{|Q_{2D_\alpha} - Q_{2D_0}|}{Q_{2D_\alpha}} \\ \text{error}_2(\%) = 100. \dfrac{|Q_{2D_\alpha} - Q_{2D_{\alpha c}}|}{Q_{2D_\alpha}} \end{cases}. \tag{21}$$

The higher the value of N_{turns}, the higher Q_{2D_α}, whereas Q_{2D_0} remains constant because no twist is geometrically introduced. For N_{turns} per meter equal to 64, the relative error is roughly 1.0549% and increases with N_{turns} because of the emergence of new capacitive coupling as elaborated in the previous section, increasing thus the discrepancy between the two.

The engineering approach adopted to correct the 2D straight values Q_{2D_0} to twisted ones $Q_{2D_{\alpha c}}$ thus gives approximate, but not precise, values of the twisted charges. Therefore, the ratio of lengths is not enough to compute the value of the twisted charge. This proves the added value of the 2D twisted model and the importance of its usage when it comes to a twisted geometry. Indeed, the proposed 2D twisted model has the same computational efficiency as the 2D straight model, does not need a post processing (i.e. correcting the

straight values with the length ratio) and fully considers the impact of the twist over the computed values.

5.2 Impact of the diameter of the conductor

To study the impact of the diameter of the conductor, N_{turns} per meter was set to 320 turns and ℓ_i to 28 μm. The diameter was varied from 0.4 to 5.16 mm. The results are seen in Figure 9.

As expected, the charges, straight and twisted, increase with the diameter of the conductor because the surface of the copper increases as well. This is illustrated in Figure. 5 and even though the two conductors are not planar, the formula for plane capacitors can be used to understand the impact:

$$C_{\text{pp}} = \frac{\varepsilon A}{\ell_i}, \tag{22}$$

where A is the surface of the parallel copper plates, which increases with d. Moreover, the two charges Q_{2D_α} and Q_{2D_0} do not increase in the same manner. This is seen in Figure 7, where the twisted geometry introduces capacitive coupling between the different parts of the twisted conductors (C_s): the higher α, the lesser the thickness of the equivalent insulation of C_s, the higher is the value of the computed charge. The values of $Q_{2D_{\alpha_c}}$ were also computed and plotted in Figure 9, where the discrepancy between $Q_{2D_{\alpha_c}}$ and Q_{2D_α} is because of the increase of the values of d, which increases the value of the length ratio (ℓ_h increases with d, whereas ℓ_e is constant because N_{turns} is constant).

5.3 Impact of the insulation thickness

Here, d was set to 0.8 mm and N_{turns} per meter to 320. The insulation thickness ℓ_i was varied from 10 to 50 μm. The results are seen in Figure 10 where a 2D geometry is presented to visualize the impact.

Following the same explanatory approach used in Section 5.2, and by making use of the parallel plate capacitive coupling analogy, the results can be easily interpreted as well.
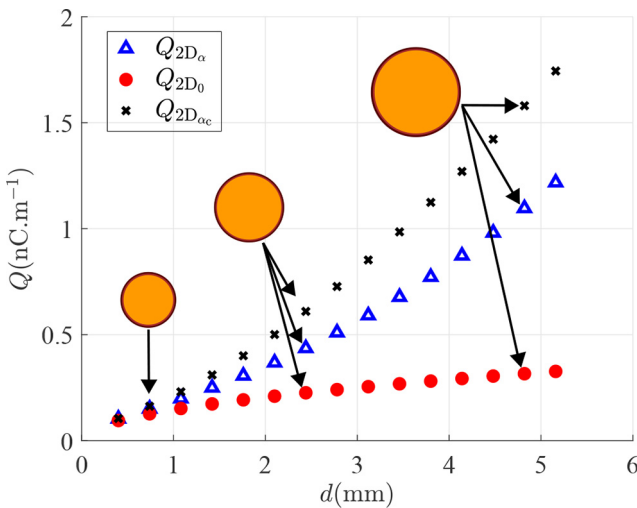

Figure 9.
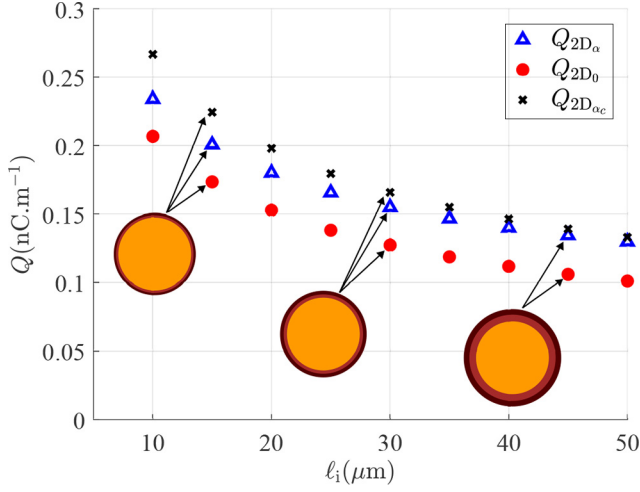Study of the impact of the diameter of the conductor on the computed charges

The capacitance (or the charge because $\Delta V = 1$ V) is inversely proportional to the thickness of the dielectric. Thus, the smaller ℓ_i, the easier the storage of the charges. For this study also, the values of $Q_{2D_{\alpha_c}}$ were computed and seem to converge to Q_{2D_α} for very high non-physical values of ℓ_i.

5.4 Study of the standard IEC 60851-5

As an application to the developed model, we propose to investigate the twist configurations in the IEC 60581-5 standard (IEC, 2019), which are summarized in Table 2.

For each diameter range d, a value of N_{turns} (ultimately α) is defined for $\ell_s = 0.125$ m, which is also fixed by the standard. The higher the value of d, the lesser the N_{turns} and the less twisted the geometry is. The performed study consists in computing for each d varying from 0.1 to 2.4 mm, ultimately the upper and lower bounds of the specified range, the 2D charges: Q_{2D_α} and Q_{2D_0}. Their variations according to d are plotted in Figure 11. The relative error was computed as in (21) (i.e. error$_1$). Here, the maximum number of turns N_{turns} per meter does not exceed 264 turn per meter (value computed for $N_{turns} = 33$) which is inferior to the values chosen in Sections 5.1–5.3.

In Figure 11, two parameters vary: the diameter d and the number of turns N_{turns}. To understand the variations, each sub-range where only one parameter varies will be studied

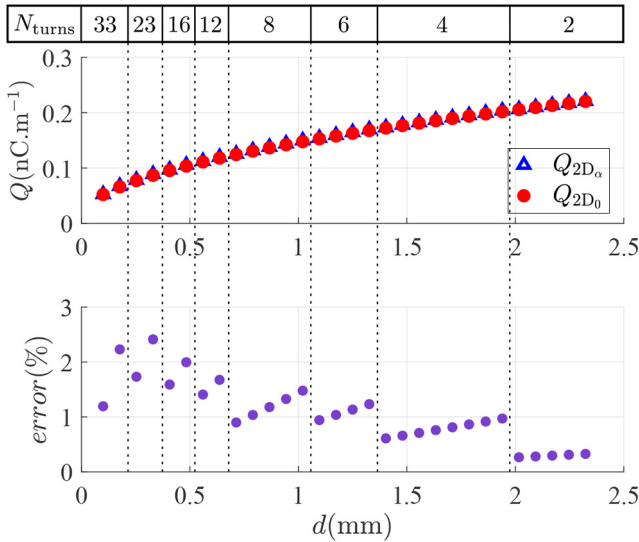| Range of the diameter (mm)	N_{turns}	N_{turns} per meter
$0.100 \leq d < 0.250$	33	246
$0.250 \leq d < 0.355$	23	184
$0.355 \leq d < 0.500$	16	128
$0.500 \leq d < 0.710$	12	96
$0.710 \leq d < 1.060$	8	64
$1.060 \leq d < 1.400$	6	48
$1.400 \leq d < 2.000$	4	32
$2.000 \leq d < 2.500$	2	16

Source: IEC (2019)

Figure 11.
Study of the standard

separately. Taking, for instance, the sub-range of d where $N_{\text{turns}} = 4$, corresponding to a diameter varying between 1.4 and 2 mm, increasing d increases simultaneously the charges (Q_{2D_α}, Q_{2D_0}) as well as the relative error between the two. This agrees well with the results of Section 5.2. Moreover, the variation of the slope of the relative error is because of the decrease of N_{turns} with the increase of the value of d. The higher the d is, the less twisted the geometry is, the smaller the value of C_s, the slighter is the difference between the twisted and straight charges until it eventually nullifies for a $N_{\text{turns}} = 0$. It should also be mentioned that in real applications, the insulation thickness ℓ_i also varies with the diameter d (IEC, 2013) which was considered constant for the study of the standard.

6. Conclusion
This paper presents an efficient method to solve a 3D twisted electrostatic problem using 2D finite elements based on a helicoidal change of coordinates. The object of study is a twisted pair widely used in different electrical engineering applications. The low time complexity of the 2D model is highlighted, as well as its high accuracy, when compared to the 3D model. The importance of using a 2D twisted geometry instead of a 2D straight geometry to study a 3D twisted problem is emphasized.

The proposed model, by inserting the correct permittivities of the dielectric materials used in real application, could efficiently provide the value of the capacitance between twisted wires. The model may even be used as an alternative to measurements, enabling the analysis of twisted wires only by simulations. The model could also be adopted for various other case studies of twisted pairs: a Debye model could, for example, be used to describe the frequency-dependent behavior of the used insulation; or the impact of the temperature over the permittivity that could also be taken into account by using, e.g. an Arrhenius model.

References

Acero, J., Lope, I., Burdío, J., Carretero, C. and Alonso, R. (2014), "Loss analysis of multistranded twisted wires by using 3D-FEA simulation", *In Proc. COMPEL, Santander, Spain*, pp. 1-6, doi: 10.1109/COMPEL.2014.6877168.

Bell, A.G. (1876), "Researches in telephony", *Proceedings of the American Academy of Arts and Sciences*, Vol. 12, pp. 1-10, doi: 10.1109/63.903993.

Bossavit, A. (1998), *Computational Electromagnetism: Variational Formulations, Complementarity, Edge Elements*, Academic Press.

Dular, P., Legros, W. and Nicolet, A. (1998b), "Coupling of local and global quantities in various finite element formulations and its application to electrostatics, magnetostatics and magnetodynamics", *IEEE Transactions on Magnetics*, Vol. 34 No. 5, pp. 3078-3081, doi: 10.1109/20.717720.

Dular, P., Geuzaine, C., Henrotte, F. and Legros, W. (1998a), "A general environment for the treatment of discrete problems and its application to the finite element method", *IEEE Transactions on Magnetics*, Vol. 34 No. 5, doi: 10.1109/20.717799.

Ern, A. and Guermond, J.-L. (2013), *Theory and Practice of Finite Elements*, Springer, Vol. 159.

Geuzaine, C. and Remacle, J.-F. (2009), "Gmsh: a 3-D finite element mesh generator with built-in pre- and post-processing facilities", *International Journal for Numerical Methods in Engineering*, Vol. 79 No. 11, pp. 1309-1331, doi: 10.1002/nme.2579.

Guastavino, F. and Dardano, A. (2012), "Life tests on twisted pairs in presence of partial discharges: influence of the voltage waveform", *IEEE Transactions on Dielectrics and Electrical Insulation*, Vol. 19 No. 1, pp. 45-52, doi: 10.1109/TDEI.2012.6148501.

Gustavsen, B., Bruaset, A., Bremnes, J.J. and Hassel, A. (2009), "A finite-element approach for calculating electrical parameters of umbilical cables", *IEEE Transactions on Power Delivery*, Vol. 24 No. 4, pp. 2375-2384.

Henrotte, F., Meys, B., Hedia, H., Dular, P. and Legros, W. (1999), "Finite element modelling with transformation techniques", *IEEE Transactions on Magnetics*, Vol. 35 No. 3, pp. 1434-1437, doi: 10.1109/20.767235.

IEC (2013), "Specifications for particular types of winding wires – part 0-1: general requirements – enamelled round copper wire", *Standard IEC60317-0-1*.

IEC (2019), "Winding wires – test methods – part 5: electrical properties", Standard IEC60851-5.

Lyly, M., Zermeno, V., Stenvall, A., Lahtinen, V. and Mikkonen, R. (2012), "Finite element simulations of twisted NbTi conductors", *IEEE Transactions on Applied Superconductivity*, Vol. 23 No. 3, pp. 6000105-6000105, doi: 10.1109/TASC.2012.2228532.

Moser, J.R. and Spencer, R.F. (1968), "Predicting the magnetic fields from a twisted-pair cable", *IEEE Transactions on Electromagnetic Compatibility*, Vol. EMC-10 No. 3, pp. 324-329, doi: 10.1109/TEMC.1968.302936.

Nicolet, A., Movchan, A.B., Guenneau, S. and Zolla, F. (2006), "Asymptotic modelling of weakly twisted electrostatic problems", *Comptes Rendus Mécanique*, Vol. 334 No. 2, pp. 91-97, doi: 10.1016/j.crme.2005.12.001.

Nicolet, A., Zolla, F., Agha, Y.O. and Guenneau, S. (2007b), "Leaky modes in twisted microstructured optical fibers", *Waves in Random and Complex Media*, Vol. 17 No. 4, pp. 559-570.

Nicolet, A., Movchan, A.B., Geuzaine, C., Zolla, F. and Guenneau, S. (2007a), "High order asymptotic analysis of twisted electrostatic problems", *Physica B: Condensed Matter*, Vol. 394 No. 2, pp. 335-338.

Paul, C.R. and Jolly, M.B. (1982), "Sensitivity of crosstalk in twisted-pair circuits to line twist", *IEEE Transactions on Electromagnetic Compatibility*, Vol. EMC-24 No. 3, pp. 359-364, doi: 10.1109/TEMC.1982.304067.

Pignari, S.A. and Spadacini, G. (2011), "Plane-wave coupling to a twisted-wire pair above ground", *IEEE Transactions on Electromagnetic Compatibility*, Vol. 53 No. 2, pp. 508-523, doi: 10.1109/ TEMC.2010.2061855.

Remacle, J., Nicolet, A., Genon, A. and Legros, W. (1994), "Comparison of boundary elements and transformed finite elements for open magnetic problems", *Transactions on Modelling and Simulation*, Vol. 7.

Waldron, R.A. (1958), "A helical coordinate system and its applications in electromagnetic theory", *The Quarterly Journal of Mechanics and Applied Mathematics*, Vol. 11 No. 4, pp. 438-461, doi: 10.1093/ qjmam/11.4.438.

Corresponding author

Guillaume Parent can be contacted at: guillaume.parent@univ-artois.fr